Chemical Engineering Journal 223 (2013) 99–109

Contents lists available at SciVerse ScienceDirect

Chemical Engineering Journal

journal homepage: www.elsevier.com/locate/cej

Formation characteristics of Taylor bubbles in a microchannel with a converging shape mixing junction

Minhui Dang [a,b], Jun Yue [a], Guangwen Chen [a,*], Quan Yuan [a]

[a] Dalian National Laboratory for Clean Energy, Dalian Institute of Chemical Physics, Chinese Academy of Sciences, Dalian 116023, China
[b] Graduate University, Chinese Academy of Sciences, Beijing 100049, China

HIGHLIGHTS

- Shear stress plays an important role in determining bubble length in squeezing regime.
- A correlation was developed to address the effect of μ_L and j_{TP} on bubble length.
- Bubble frequency reaches a maximum with an increase of the gas–liquid flow ratio.
- Cross-sectional shape of Taylor bubbles is close to square at low *Ca*.

ARTICLE INFO

Article history:
Received 28 October 2012
Received in revised form 21 February 2013
Accepted 26 February 2013
Available online 14 March 2013

Keywords:
Microchannel
Hydrodynamics
Taylor flow
Bubble
Microreactor

ABSTRACT

The bubble formation in a square microchannel with a converging shape mixing junction has been investigated under gas–liquid Taylor flow using a high-speed camera. A typical bubble formation process was found to consist of two steps including the expansion and rupture steps. The bubble length could be approximated as the product of the rupture time and two-phase mixture velocity. Significant influence of liquid viscosity and two-phase mixture velocity on the bubble length was observed, although a linear dependence of the bubble length on gas–liquid flow ratio is present for a given two-phase mixture velocity or liquid viscosity. This indicates that shear stress plays an important role in determining the bubble length in the current microfluidic device even at low Capillary numbers where the squeezing regime is expected to predominate. An empirical correlation expressing the bubble length as a function of gas–liquid flow ratio, liquid viscosity and two-phase mixture velocity was developed to describe the experimental results. The bubble frequency was found to reach a maximum as gas–liquid flow ratio is increased from 0.5 to 1. The cross-sectional shape of Taylor bubble was close to be square at low capillary numbers, which is in agreement with the literature results.

1. Introduction

During the past two decades, microreactor technology has become one of the important techniques of process intensification for the chemical and process industry [1], primarily owing to efficient heat and mass transfer properties offered by this technology for chemical production. Its application potential has been demonstrated in many areas, such as mixing [2,3], separations [4,5], reactions [6–8] and chemical analysis [9].

Mass transfer and reaction performance in gas–liquid microreactors are highly dependent on hydrodynamics of gas–liquid flow therein. Taylor flow is one common flow pattern encountered during gas–liquid flow through microchannels [10], which consists of sequences of an elongated bubble and a liquid slug. The bubble length is usually several times of the channel diameter. The liquid slugs are separated by the bubbles and the two adjacent liquid slugs are connected only through a thin film (if present) between the bubble and the channel wall, which indicates a significant reduction in axial mixing [11]. The recirculation in the liquid slugs improves radial mixing [12,13]. Thus, microreactors operated under Taylor flow have found great use in various chemical processes such as nanoparticle synthesis [14–17] and homogeneously/heterogeneously catalyzed gas–liquid reactions [18–20].

The successful design of microreactors operated under Taylor flow relies on a full understanding on its hydrodynamics [21]. In order to manipulate Taylor flow precisely, it is necessary to investigate the formation process of Taylor bubbles. Various formation mechanisms have been proposed. Garstecki et al. [22] proposed the squeezing mechanism in T-type microfluidic junction geometries that controls the bubble formation at low Capillary numbers (e.g., $Ca < 10^{-2}$), where interfacial force is expected to be dominant over shear stress. Under this regime, the break-up of a Taylor

* Corresponding author. Tel.: +86 411 8437 9031; fax: +86 411 8469 1570.
E-mail address: gwchen@dicp.ac.cn (G. Chen).
URL: http://www.microchem.dicp.ac.cn (G. Chen).

1385-8947/$ - see front matter © 2013 Elsevier B.V. All rights reserved.
http://dx.doi.org/10.1016/j.cej.2013.02.108

Nomenclature

Ca	Capillary number defined by ($Ca = \mu_L j_{TP}/\sigma$), dimensionless
d_h	hydraulic diameter (m)
f_B	bubble frequency (s^{-1})
h	height of the microchannel (m)
j_G	superficial gas velocity (m/s)
j_L	superficial liquid velocity (m/s)
j_{TP}	two-phase mixture velocity defined by ($j_{TP} = j_G + j_L$) (m/s)
L_B	length of Taylor bubble (m)
Q	volumetric flow rate (m^3/s)
r_{3D}	equivalent radius of the bubble (m)
Re	Reynolds number defined by ($Re = d_h j_{TP}\rho_L/\mu_L$), dimensionless
t	time (s)
τ	shear stress defined by ($\tau = \mu_L\gamma$) (Pa)
V	volume (m^3)
w	width of the main microchannel (m)
w_B	width of the bubble (m)
w_g	width of inlet microchannel for gas (m)

Greek letters

γ	shear rate (s^{-1})
ε	hold-up, dimensionless
θ	angle, degree
μ	viscosity (Pa s)
ρ	density (kg/m^3)
σ	surface tension (N/m)

Subscripts

B	Taylor bubble
e	expansion step
G	gas phase
$inlet$	inlet microchannel of gas or liquid
L	liquid phase
max	maximal
r	rupture step
ref	reference properties
TP	two-phase mixture

bubble is controlled by the liquid-phase pressure drop across the emerging bubble resulting from its blockage of the liquid flow path. De Menech et al. [23] investigated the formation of droplets in T-type junction microchannels by numerical simulation and found three regimes depending on the magnitude of Ca, i.e., the squeezing, dripping and jetting regimes. Recently, the central ideas of squeezing mechanism have been confirmed experimentally by Abate et al. [24] who utilized Laplace sensors to perform a detailed analysis of pressure fluctuations generated during drop formation in a T-type junction. They further found that even at the highest Ca under investigation (i.e., $Ca = 0.21$), squeezing still played a role although shear stress was more important in drop formation.

Besides the formation mechanisms, the length of Taylor bubble has also been extensively studied because of its importance in determining pressure drop and mass transfer rate under Taylor flow [25–27]. Table 1 summarizes the existing literature correlations proposed for the prediction of Taylor bubble length in microchannels. For the T-type junction microchannel, Garstecki et al. [22] formulated Eq. (1) according to the squeezing mechanism, which could predict the bubble length formed in the liquid containing surfactants. Qian and Lawal [28] obtained Eq. (2) to estimate the bubble length by CFD simulation. The correlation shows that the bubble length depends mainly on the phase holdup, but slightly on Reynolds number (Re) and Capillary number (Ca). van Steijn et al. [29] investigated liquid-phase flow field during bubble formation in the squeezing regime by microscopic particle image velocimetry (μ-PIV). They confirmed the scaling law of Garstecki et al. [22] and obtained Eq. (3). De Menech et al. [23] also verified numerically the presence of squeezing regime (Eq. (4)). In the dripping regime, the authors gave a correlation (Eq. (5)) to predict droplet size that depends on Ca and shear rate. Tan et al. [30] derived Eq. (6) to predict the bubble length considering the influence of the angle of gas and liquid inlet channels, gas–liquid flow ratio (j_G/j_L) and Ca. Eq. (7) was derived for a microchannel with a high aspect ratio by Xiong and Chung [31]. They found that the bubble length was dependent on j_G/j_L and Re. Fu et al. [32] proposed three correlations (Eqs. (8)–(10)) to predict bubble length produced in the squeezing, transition and dripping regimes, respectively. For the cross-shape junction microchannel, Cubaud et al. [33] found a linear relationship (Eq. (11)) between the bubble length and the reciprocal of the liquid fraction (α_L). Dietrich et al. [34] developed a correlation (Eq. (12)) for the bubble length in which the effect of liquid viscosity (μ_L), surface tension, j_G/j_L and the angle of liquid phase inlet channels was addressed. Fu et al. [35] further proposed Eq. (13) to estimate bubble length considering the influence of j_G/j_L and μ_L.

The above correlations to a large extent reveal the dependence of bubble length on the operating conditions, fluid properties and different inlet geometries, most of which were established based on the squeezing mechanism proposed by Garstecki et al. [22]. However, it will be shown in this work that the predictions of the existing correlations are overall not satisfactory in the current microchannel with a converging shape mixing junction, especially at large j_G/j_L. For the same j_G/j_L and gas–liquid system, we observed that bubble length varies greatly when changing the two-phase mixture velocity, which cannot be simply interpreted based on the scaling law of Garstecki et al. [22]. Our results reveal that shear stress plays an important role in determining the bubble length even at low Ca where the squeezing regime is expected to predominate.

In this work, we investigate experimentally the bubble formation process in a microchannel with a converging shape mixing junction. The converging shape mixing geometry is expected to introduce a smaller pressure drop in the junction than the cross-shape mixing geometry. A further advantage using covering shape mixing geometry might be that the microchannel wall tends to be preferentially wetted by the liquid at the initial start-up, thus facilitating the formation of regular Taylor bubbles. The main purpose here is to examine the effect of j_G/j_L, two-phase mixture velocity (j_{TP}) and μ_L on the expansion and rupture steps of a Taylor bubble in detail and thus to provide insights on the length of bubbles produced in such microfluidic geometry at relatively low Ca. An empirical correlation for bubble length is thus developed to describe the experimental results. Furthermore, the bubble frequency and bubble shape are also studied.

2. Experimental

2.1. Materials

Air was used as the gas phase. Aqueous solutions with different contents of glucose were utilized as the liquid phase (Kermel, China). Glucose was used to change the viscosity of the liquid phase. A

Table 1
Literature correlations on bubble length in Taylor flow through microchannels.

Authors	Channel shape and size	Inlet mixing geometry	Operational condition	Correlation	
Garstecki et al. [22]	Rectangular w: 50, 100, 200 μm h: 33 μm w_g: 50, 100 μm	T-type junction	j_G/j_L: 0.5–3 $Ca < 0.01$	$\frac{L_B}{w} = 1 + \alpha\frac{j_G}{j_L}$ $a \approx 1$ for $w_g/w \geqslant 1/2$ and $h \leqslant w$	(1)
Qian and Lawal [28][a]	Rectangular (2D) w: 250, 500, 750, 1000, 2000 and 3000 μm	T-type junction	j_G/j_L: 0.1–10 Ca: 2.78×10^{-3}∼0.01 Re: 15–1500	$\frac{L_B}{w} = 1.637\varepsilon_G^{0.107}(1-\varepsilon_G)^{-1.05}Re^{-0.075}Ca^{-0.0687}, \varepsilon_G = \frac{j_G}{j_G+j_L}$	(2)
van Steijn et al. [29]	Square w (h): 800 μm	T-type junction	j_G/j_L: 0.6–5	$\frac{L_B}{w} = 1.5 + 1.5\frac{j_G}{j_L}$	(3)
De Menech et al. [23][a,b]	Square w (h): not specified	T-type junction	Squeezing regime j_G/j_L: 0–2 $Ca < 0.01$	$\frac{V_B}{w^3} = 1 + 2\frac{j_G}{j_L}$	(4)
			Dripping regime $Ca > 0.02$	$\frac{V_B}{w^3} = \frac{1}{(Ca\gamma w/j_L)^{0.4}}$	(5)
Tan et al. [30]	Rectangular w: 500 μm h: 400 μm θ_{inlet}: 30, 60, 90, 120, 150°	T-type junction	j_G/j_L: 0.3–10 $Ca < 0.012$	$\frac{L_B}{w} = \frac{1}{2}\left(\frac{j_G}{j_L \sin\theta_{inlet}} + \frac{2}{3}\cot\theta_{inlet}\right)^{1/2}Ca^{-1/5}$	(6)
Xiong and Chung [31]	Rectangular w: 594 μm h: 80 μm	T-type junction	j_G/j_L: 0.1–3.33	$\frac{L_B}{w} = 1 + 1.724Re^{0.173}\left(\frac{j_G}{j_L}\right)^{0.797}$	(7)
Fu et al. [32]	Rectangular	T-type junction	Squeezing regime Ca: 10^{-4}–5.8×10^{-3}	$\frac{L_B}{w} = 0.32\frac{j_G}{j_L} + 0.64$	(8)
			Transition regime	$\frac{(L_B w_B)^{0.5}}{w} = 0.26\left(\frac{j_G}{j_L}\right)^{0.18}Ca^{-0.25}$	(9)
	w: 120 μm h: 40 μm		Ca: 0.0058–0.013		
			Dripping regime Ca: 0.013–0.1	$\frac{r_{3D}}{h} = 0.71Ca^{-0.11}, \quad r_{3D} = \sqrt[3]{\frac{3V}{4\pi}}, \quad V = \frac{\pi L_B w_B h}{6}$	(10)
Cubaud et al. [33]	Square w (h): 100 μm	Cross-shape junction	j_G/j_L: 0–9	$L_B = h\alpha_L^{-1}, \alpha_L = \frac{j_L}{j_L+j_G}$	(11)
Dietrich et al. [34]	Square w (h): 600, 1000 μm w_g: 200, 500, 1000 μm θ_{inlet}: 60°, 90°, 180°	Converging shape or cross-shape junction	j_G/j_L: 10^{-6}–10 Re: 0.005–950	$\frac{L_B}{w_g} = 8.3\left(\frac{\theta_{inlet}}{\theta_{inlet}^{max}}\right)^{-1/8}\left(\frac{\sigma}{\sigma_{ref}}\right)\left(\frac{\mu}{\mu_{ref}}\right)^{1/10}\left(\frac{j_G}{j_L}\right)^{1/4}$ $\theta_{inlet}^{max} = 180°$	(12)
Fu et al. [35]	Square w (h): 400, 600 μm	Cross-shape junction	j_G/j_L: 0.1–4 $Ca < 0.1$ Re_L: 0.66–144.93	$\frac{L_B}{w} = 1.40\left(\frac{j_G}{j_L}\right)^{1.10}Re_L^{0.46}$ $Re_L = \rho_L j_L w/\mu_L$	(13)

[a] These studies are based on numerical simulation; the others are based on experimental measurements.
[b] Only bubble volume was given. The bubble length was not specified.

Table 2
Properties of liquids used in this work.

Liquid phase	Density, ρ	Viscosity, μ	Surface tension, σ
	(kg m^{-3})	(m Pa s)	(mN m^{-1})
Water	1000	1.00	72.6
36 wt.% glucose in water	1100	4.42	73.3
45 wt.% glucose in water	1180	9.83	75.3

viscometer (DV-II+Pro, Brookfield, USA) was employed to characterize liquid viscosity. Surface tension was measured using a tensiometer (OCA15 EC, Dataphysics, Germany) by the pending drop method. Table 2 summarizes properties of liquids used in the experiments.

2.2. Microchannel device

Microchannels were fabricated on a polymethyl methacrylate (PMMA) plate by micromachining technology (FANUCKPC-30a) in our Machining Center, which was sealed with another thin PMMA plate using screw fittings through the punched holes on the peripheries of both plates in order to form a closed microchannel section for fluid passage. Fig. 1a shows the schematic of the microchannel device, where a central inlet microchannel was used for the introduction of the dispersed gas phase and two side inlet microchannels for the introduction of the continuous liquid phase. The angle between each side inlet microchannel and the central inlet microchannel is 30°. Taylor flow was generated in the main microchannel. All microchannels have a square cross-section (0.6 mm × 0.6 mm). The lengths of three inlet microchannels and the main microchannel are 26 mm and 48 mm, respectively.

2.3. Experimental setup

The schematic of the experimental setup is shown in Fig. 1b. Gas was provided from an air cylinder. Prescribed flow rate of air was adjusted by a mass flow controller with a flow range of 0–50 ml/min (SevenStar, D07-7B). The air stream was directly fed into the central inlet microchannel of the device that was placed horizontally and the static pressure in the gas feeding line was measured by a pressure transducer with a range of 0–100 kPa

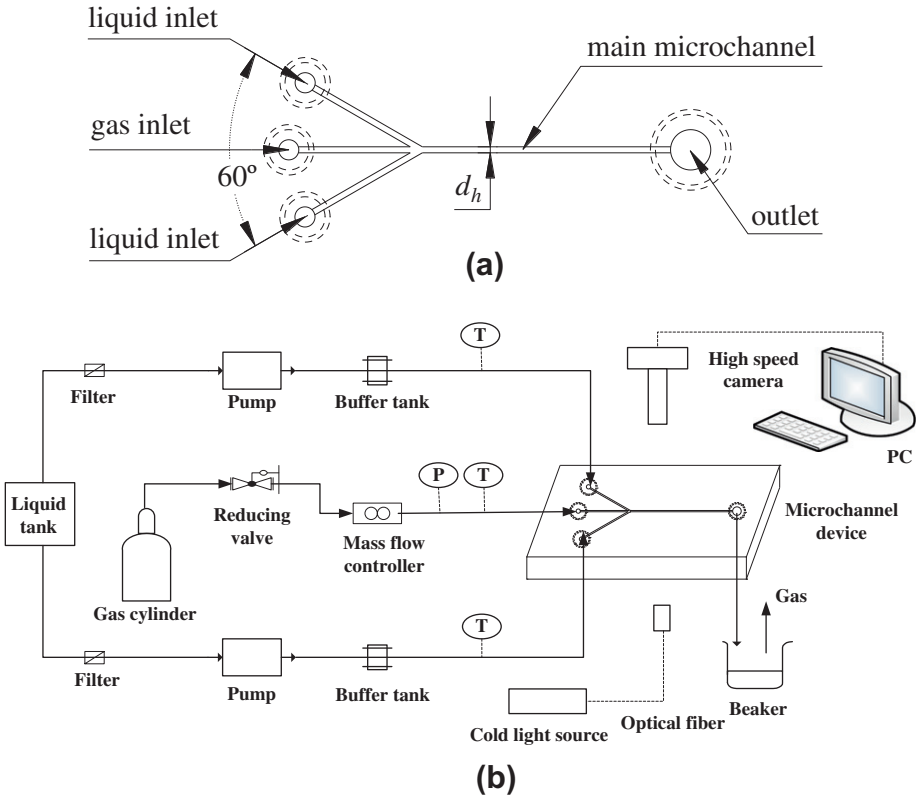

Fig. 1. Schematic of (a) the microchannel device; and (b) the experimental setup.

(Nokisens, CEMPX213). Liquid was stored in a tank. After flowing through the filters to remove contaminations, the liquid was delivered by two digital pumps with a range of 0–10 ml/min (LabAlliance, Series II Digital Pump) into two side inlet microchannels. Three thermocouples (K-type) were located in the inlet ports to measure the corresponding temperatures. All experiments were conducted under ambient conditions (0.1 MPa, 19–21 °C).

The system was run for at least 5 min in order to reach a steady state under a given flow rate. For each operational condition, experiments were carried out at least thrice and the relative error in the obtained bubble length between the measurements was found to be within 5%. During the experiments, a high-speed CMOS camera (Basler, A504kc) connected to a computer placed above the contactor was employed to record the images of Taylor flow in the main microchannel. The camera was further equipped with a megapixel lens (Nikon, AF35/2D) as well as a set of extension tubes in order to magnify a section of the microchannel under investigation. The light needed for the illumination of the microchannel was provided by a cold fiber light (SCHOTT, DCR III) which was placed beneath the microchannel. Under each operating condition, lengths of Taylor bubbles were measured from the corresponding images. At least 10 images were analyzed to give the average value of Taylor bubble length (L_B). The bubble formation frequency, f_B, was calculated from these images by dividing the number of bubbles captured by the time elapsed.

3. Results and discussion

3.1. Formation process of Taylor bubble

To understand the key parameters that control the bubble formation process, a study was devoted to observing the influence of liquid viscosity, gas–liquid flow ratio and two-phase mixture velocity. In our experiments, μ_L, j_G/j_L and j_{TP} ranged from 1.00 to 9.83 m Pa s, from 0 to 2.5 m/s, and from 0 to 3.6 m/s, respectively. Fig. 2 shows the Taylor bubble formation process during one period, from which a typical bubble formation process consists of two steps. Firstly, after the pinch-off of the preceding bubble, the emerging bubble expands axially and radically until its tip blocks the entrance of main channel (Fig. 2a–c). This step is called as the expansion step and its corresponding time is named as the expansion time, t_e. Secondly, the axial velocity component of the liquid from two side inlet microchannels which parallels the main channel, along with the gas dynamic pressure, drives the emerging bubble into the main microchannel under the action of shear stress. The pressure difference across the gas–liquid interface squeezes the emerging bubble to form a neck at the mixing junction until the neck eventually ruptures (Fig. 2d–h). This step is called as the rupture step and the time of duration is named as the rupture time, t_r.

According to the fluid dynamic theory, both the expansion and rupture steps of a bubble are related to the competition among various forces exerted on the emerging bubble, such as surface tension ($\Delta P_\sigma \approx 2\sigma/(d_h/2)$), shear stress ($\tau \approx \mu_L\gamma$) and dynamic pressure (inertial forces, $\Delta P_G \approx \rho_G j_G^2/2$, $\Delta P_L \approx \rho_L j_L^2/2$) [34,35]. The surface tension always hinders the expansion and the rupture of the emerging bubble. The shear stress depends on the shear rate on the gas–liquid interface and the liquid viscosity, which is expected to accelerate both steps. The gas dynamic pressure accelerates the expansion process of the forming bubble. The liquid dynamic pressure suppresses the expansion process whereas it accelerates the rupture process. It is worth mentioning that the influence of buoyancy force can be neglected in microchannels due to small channel dimensions involved.

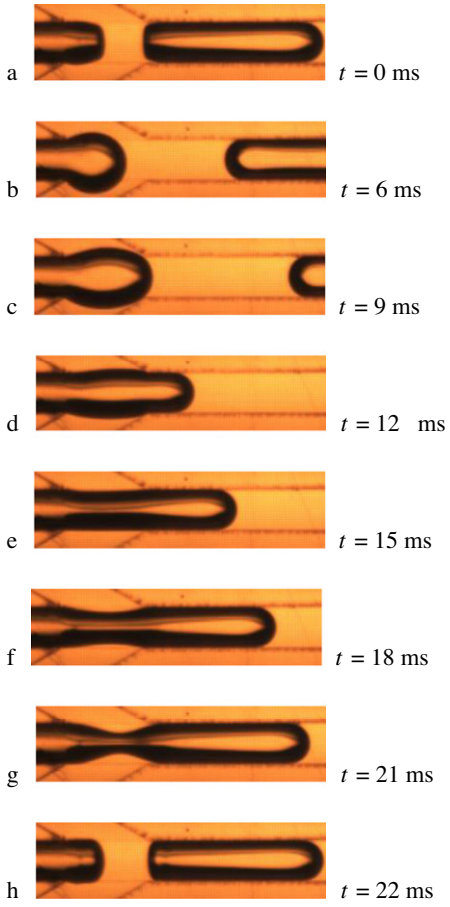

Fig. 2. Taylor bubble formation process during one period. Gas phase: air; liquid phase: water. j_G = 0.112 m/s, j_L = 0.108 m/s, and d_h = 600 μm.

3.1.1. Effect of liquid viscosity on the expansion time and the rupture time

From Fig. 3a, it is seen that the influence of liquid viscosity can be easily discerned especially at low values of j_G/j_L. An increase in liquid viscosity tends to decrease the expansion time for a given j_G and j_L, which is due to the action of the shear stress that the liquid exerts on the emerging bubble body facilitating its expansion [36]. At elevated j_G/j_L, such influence of liquid viscosity is obscured by the prevailing effect of relatively high j_G which decreased the expansion time to a substaintially low level.

Fig. 3b shows that the rupture time is significantly decreased with the increase of liquid viscosity. At the beginning of the rupture step, the front of the emerging bubble is thought to be almost spherical which cannot completely block the main microchannel (of square cross section). So the liquid can still flow through the gap between the emerging bubble and the microchannel wall. As the velocity of the liquid flowing in the gap is expected to be larger than that of the emerging bubble at this time, a somewhat significant shear stress caused by such relatively large velocity difference at the interface would act on the emerging bubble that speeds up the rupture of the bubble, which is especially the case at large liquid viscosity. This assertion is supported by the work of van Steijn et al. [29]. They measured the liquid-phase velocity in the gap between the emerging bubble and the wall of the main microchannel with a T-type mixing geometry using μ-PIV and found that the maximum liquid velocity in the plane close to the microchannel bottom was roughly four times the average velocity. Fu et al. [37] also found that the increase of liquid viscosity accelerates the formation of bubble by intensifying the shear stress.

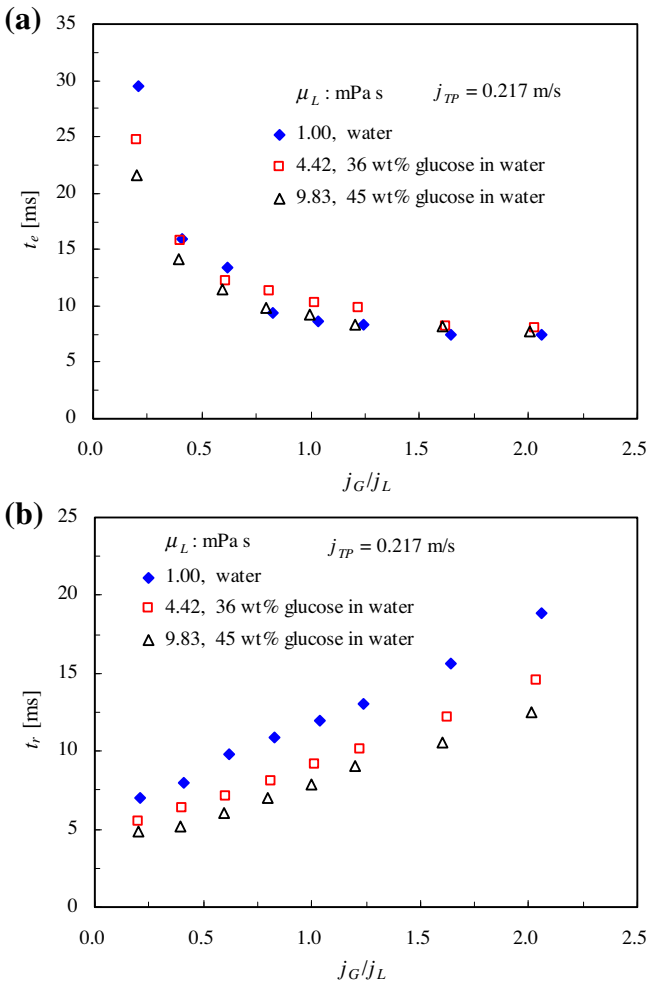

Fig. 3. Effect of liquid viscosity on (a) the expansion time and (b) the rupture time.

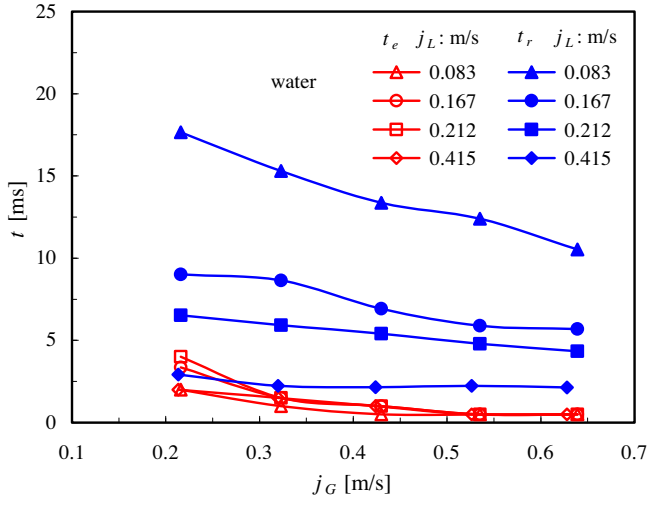

Fig. 4. Effect of superficial gas and liquid velocities on the expansion time and the rupture time.

However, when the emerging bubble body travels into the main microchannel, the cross-section of bubble body could be approximated as almost square (the bubble shape will be further discussed on Section 3.4) and the effect of shear stress may become

somewhat less significant due to more reduced flow of liquid around the channel circumference.

3.1.2. Effect of superficial gas and liquid velocities on the expansion time and the rupture time

Fig. 4 shows the effect of superficial gas and liquid velocities on the expansion time (t_e) and the rupture time (t_r). It is found that t_e decreases with an increase of the superficial gas velocity (j_G). This result indicates that the bubble tip blocks the inlet of main microchannel more quickly as j_G increases at a given superficial liquid velocity (j_L). From Fig. 4, it is seen that at the lowest j_G of 0.213 m/s, t_e increases as j_L increases from 0.083 to 0.212 m/s ($j_G/j_L > 1$). This is because that the increase of liquid dynamic pressure ($\Delta P_L \approx \rho_L j_L^2/2$) in the front of the emerging bubble with an increase in j_L baffles the expansion progress of the bubble. This is in line with the observation of Tsuge et al. [38] and Yoo et al. [39]. They found that the volume of bubbles formed from a submerged orifice decreases with an increase in system pressure. However, t_e is seen to decrease with an increase of j_L from 0.212 to 0.415 m/s ($j_G/j_L < 1$), the reason of which is still unclear.

For a given j_L, t_r generally decreases with increasing j_G because the increase of gas dynamic pressure ($\Delta P_G \approx \rho_G j_G^2/2$) speeds up the rupture of the neck of the emerging bubble. In other words, the quicker the bubble body moves into the channel, the faster the neck ruptures. And t_r decreases with the increase of j_L for a given j_G, which is because that the liquid dynamic pressure on the neck of the emerging bubble increases with the increase of j_L. According the squeezing mechanism [22], this building pressure is mainly responsible for the bubble break-up, which therefore makes the rupture of the neck easier at higher liquid dynamic pressure.

3.1.3. Effect of gas–liquid flow ratio and two-phase mixture velocity on the expansion time and the rupture time

Fig. 5a depicts the effect of gas–liquid flow ratio and two-phase mixture velocity (j_{TP}) on the expansion time for an example case with water as the liquid phase. t_e decreases gradually with the increase of gas–liquid flow ratio at a fixed j_{TP} for a given gas–liquid system, which is more pronounced when $j_G/j_L < 1$. Under such conditions, the obstructive effect of liquid dynamic pressure decreases and the promotional effect of gas dynamic pressure increases on the velocity of the bubble expansion with increasing j_G/j_L. This figure also shows that t_e decreases with increasing j_{TP} at a given j_G/j_L. This further illustrates that j_G has a greater effect on t_e than j_L.

The rupture time seems to be a linear function of gas–liquid flow ratio for a fixed mixture velocity (cf. Fig. 5b). The slope of the line of t_r versus j_G/j_L decreases when j_{TP} is increased. This means that for a given j_G/j_L the higher j_{TP}, the lower t_r. Comparing Fig. 4 with Fig. 5b, it can be seen that t_r decreases with an increase of j_G/j_L at a fixed j_L whereas it increases with an increase of j_G/j_L at a fixed j_{TP} for a given gas–liquid system. This indicates that j_L has a more pronounced effect on t_r than j_G, which is because that the rupture of the emerging bubble is mainly controlled by the squeezing of the gas neck by the pressure built up in the liquid. That is, the lower j_L, the higher t_r.

3.2. Length of Taylor bubble

3.2.1. Effect of gas–liquid flow ratio and liquid viscosity on the length of Taylor bubble

From Fig. 6, it can be seen that at a fixed two-phase mixture velocity, the bubble length increases linearly with the increase of gas–liquid flow ratio for a given liquid viscosity. But the slope of the line of L_B/d_h versus j_G/j_L changes slightly with the viscosity. The increase of liquid viscosity leads to a slight decrease in the bubble length. This is because that the rupture time was smaller when the liquid phase presents a relatively higher viscosity

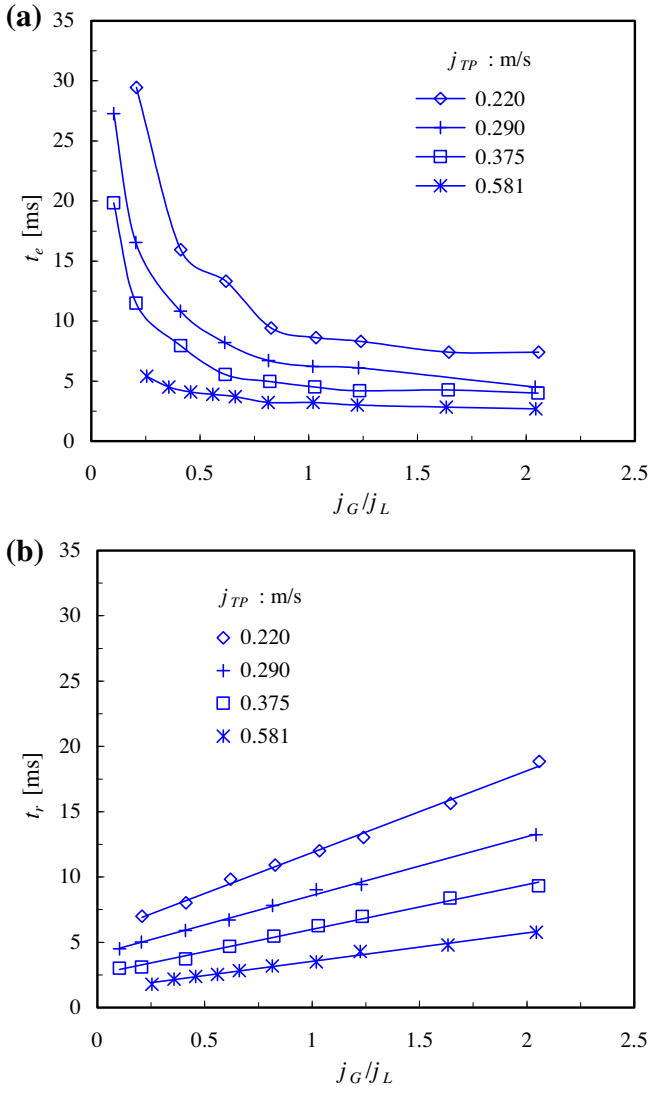

Fig. 5. Effect of gas–liquid flow ratio and two-phase mixture velocity on: (a) the expansion time; and (b) the rupture time. Liquid phase: water.

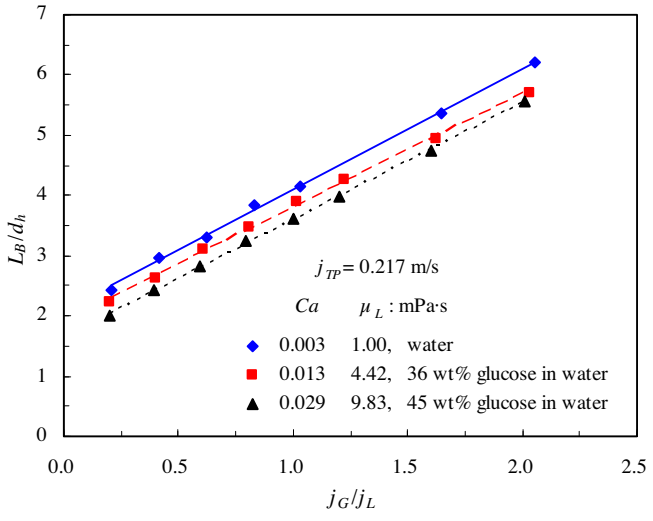

Fig. 6. Effect of gas–liquid flow ratio and liquid viscosity on the bubble length.

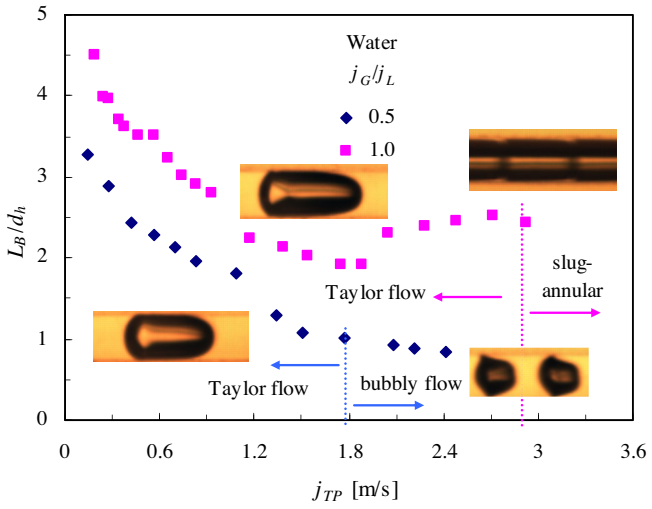

Fig. 7. Effect of two-phase mixture velocity on the bubble length for j_G/j_L = 0.5 and 1.0. Liquid phase: water.

(Fig. 3b). Therefore, the observations here suggest that the bubble length could be predicted using correlations similar to that proposed by Garstecki et al. [22], if the influence of viscosity has been well taken into account. In other words, the bubble formation is controlled by the squeezing mechanism, but shear stress also seems to have a role to play.

3.2.2. Effect of two-phase mixture velocity on the length of Taylor bubble

Fig. 7 represents the influence of two-phase mixture velocity on the bubble length for different liquid phases under investigation. It is seen that at j_G/j_L = 0.5, the bubble length decreases with the increase of j_{TP} until at j_{TP} > 1.8 m/s under which the flow pattern transforms from Taylor flow to bubbly flow. At j_G/j_L = 1.0, the bubble length decreases with increasing j_{TP} when j_{TP} < 1.9 m/s, however, it slightly increases with the increase of j_{TP} when 1.9 m/s < j_{TP} < 2.7 m/s. Then at j_{TP} > 2.9, the flow pattern is changed from Taylor flow to slug–annular flow. A clear observation from Fig. 7 is that even at low j_{TP}, its influence is significant on the bubble length. The decrease of Taylor bubble length with increasing j_{TP} can be explained by the fact that the increase of j_{TP} strengthens the shear stress ($\tau \approx \mu_L \gamma$) exerted on the emerging bubble by increasing shear rate, resulting in smaller bubbles at higher j_{TP} for the same j_G/j_L.

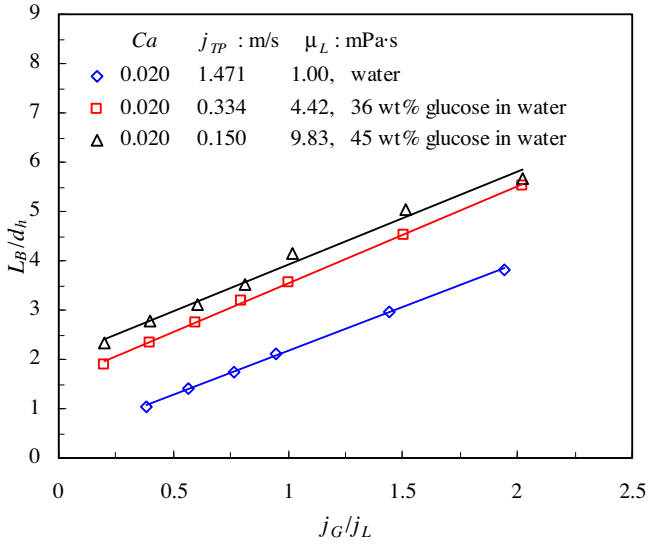

Fig. 8. Comparison between effects of liquid viscosity and two-phase mixture velocity on the bubble length.

It is further shown from Fig. 7 that the bubble length is larger at higher j_G/j_L for the same j_{TP}. This is because that for a given system, the bubble length is determined by the magnitude of t_r and j_{TP}, that is, $L_B \approx t_r \times j_{TP}$ (see Eq. (14) below). Then it can be explained based on the observation in Fig. 5b which shows that t_r increases with the increase of j_G/j_L if j_{TP} is being kept constant for a given system.

Therefore, the bubble length formed in the present microchannel is dependent not only on gas–liquid flow ratio and liquid viscosity, but also on two-phase mixture velocity.

3.2.3. Comparison between effects of liquid viscosity and two-phase mixture velocity on the length of Taylor bubble

Figs. 6 and 7 have already shown that at a fixed j_G/j_L, the bubble length decreases with an increase in μ_L for a given j_{TP} or with an increase in j_{TP} for a given μ_L. However, it appears from Fig. 8 that at a fixed Ca ($Ca = \mu_L j_{TP}/\sigma$), the bubble length increases with the increase of μ_L although it still decreases with the increase of j_{TP} for the same j_G/j_L. Note that surface tension with all three liquids under investigation is very close (see Table 2). Therefore it can be deduced that j_{TP} has a more pronounced effect on the bubble length than μ_L.

3.2.4. Empirical correlation for bubble length prediction

As shown in Fig. 9, the bubble length was found to be well approximated by the product of the rupture time and two-phase mixture velocity. That is,

$$L_B/d_h = t_r j_{TP}/d_h \quad (14)$$

Our measurements do show that the average velocity of the emerging bubble head (U_{head}) almost equals to two-phase mixture velocity (see Fig. 10), which justifies the use of Eq. (14) in the prediction of the bubble length.

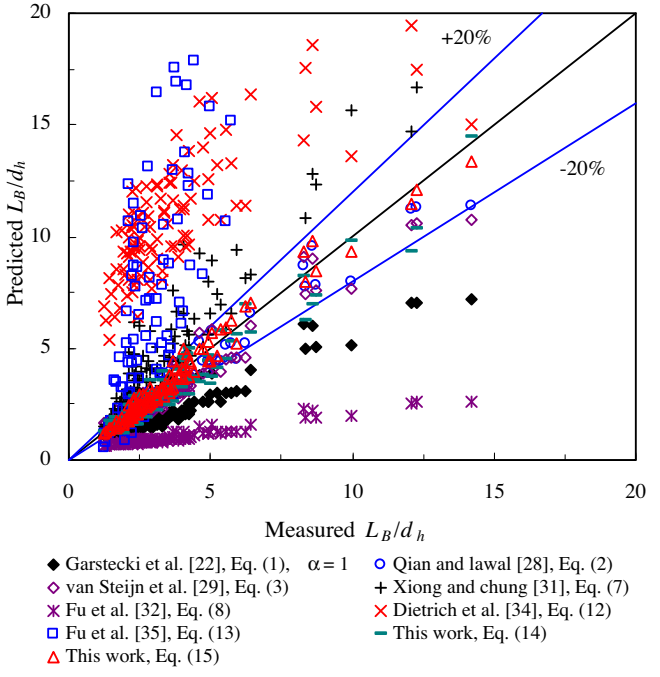

Fig. 9. Comparison between the measured (L_B/d_h) values and the predictions of literature correlations. The solid line represents the line of parity.

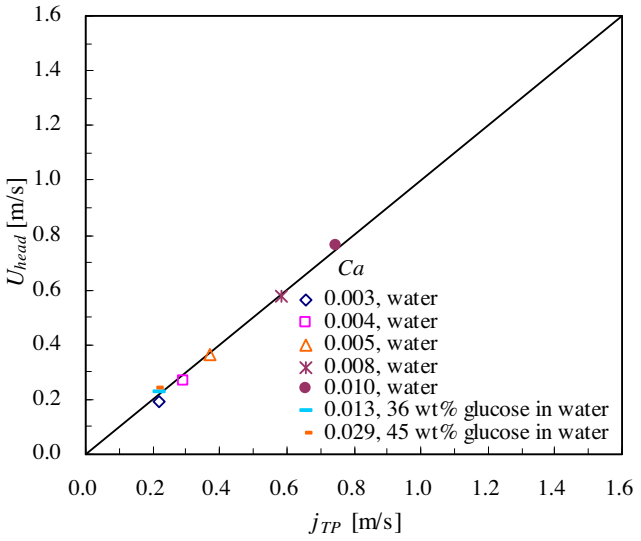

Fig. 10. Comparison between j_{TP} and U_{head}. Liquid phase: water, 36 wt.% glucose solution in water (μ = 4.42 m Pa s), 45 wt.% glucose solution in water (μ = 9.83 m Pa s). The solid line represents the line of parity.

Although the influence of various parameters including liquid viscosity, gas–liquid flow ratio and two-phase mixture velocity on the rupture time has been revealed to some extent in this work, an explicit equation address this influence is still not available. And since Eq. (14) cannot be conveniently used for the estimation of the bubble length produced in the current microfluidic geometry, we further propose the following empirical relation on the basis of Eq. (1) by correlating a total of 104 sets of experimental data:

$$\frac{L_B}{d_h} = \left(1 + 1.71\frac{j_G}{j_L}\right)\left(\frac{j_{TP}}{j_{ref}}\right)^{-0.28}\left(\frac{\mu_L}{\mu_{ref}}\right)^{-0.06} \quad (15)$$

where j_{ref} is 1 m/s and μ_{ref} is the viscosity of water as a reference. Fig. 9 shows that Eq. (15) can describe the measured L_B/d_h data fairly well, the relative error in the prediction being within ±8.3% (j_G/j_L = 0.09–6.16, μ_L/μ_{ref} = 1–9.83, j_{TP}/j_{ref} = 0.14–1.12). However, as only one microchannel was studied in this work, the impact of diameter and inlet angle on the bubble length cannot be reflected through Eq. (15) and therefore its applicability to microchannels with different dimensions still needs to be examined. Moreover, this correlation does not consider the impact of surface tension given by the fact that surface tension seems to have no significant effect on the bubble length in our experimental conditions. Similar results showing negligible influence of surface tension on the bubble length produced in the squeezing regime can be also found in the literature [22,35,37,40]. For example, Fu et al. [37] pointed out that the surface tension measured under static conditions could be irrelevant to a fast and dynamical phenomenon for bubble formation. It may be noted that there also exist contradictory findings, among which Qian and Lawal [28] found that the bubble length slightly increases with an increase of surface tension and somewhat decreases with the contact angle of the liquid to the wall from 0° to 90° according to the results of numerical simulation in a T-type microfluidic junction. This means that an increase in surface tension or the contact angle of liquid phase to wall tends to have an opposite influence on the bubble length.

Fig. 9 also gives a comparison between the experimental measurements and the predictions of the existing correlations for estimating the bubble length as detailed in Table 1. It can be seen that Eq. (1) (with α = 1), Eqs. (3) and (8) all underestimate the experimental values whereas Eqs. (7) and (13) tend to overestimate. One important reason for this discrepancy is the different inlet configurations involved. Furthermore, the effect of parameters such as liquid viscosity has not been fully investigated in some studies [22,29,31,32,35], which may also lead to somewhat poor accuracy of their correlations in the prediction. One of the inlet configurations investigated by Dietrich et al. (2008) is similar to that used in this work. Their correlation, Eq. (12), includes the effect of inlet configuration, liquid viscosity, surface tension and gas–liquid flow ratio. However, the impact of two-phase mixture velocity was not taken into account. According to Eq. (12), the bubble length should be the same at a fixed gas–liquid flow ratio for a given gas–liquid system and inlet geometry. Our results indicate that the bubble length under such conditions could vary significantly if j_{TP} is being increased (e.g., see Fig. 7). This may be a reason for a somewhat large deviation observed in the prediction of Eq. (12) compared with our experimental data. From Fig. 9, it is further shown that the predictions of Eq. (2) are in good agreement with the experimental results. This might be because that Eq. (2) fully contains the impact of liquid viscosity, surface tension and two-phase mixture velocity although it was actually derived for a T-type microfluidic junction.

3.3. Frequency of Taylor bubble

It is seen from Fig. 11a that for a given j_{TP}, the bubble frequency (f_B) first increases with the increase of j_G/j_L when j_G/j_L is smaller

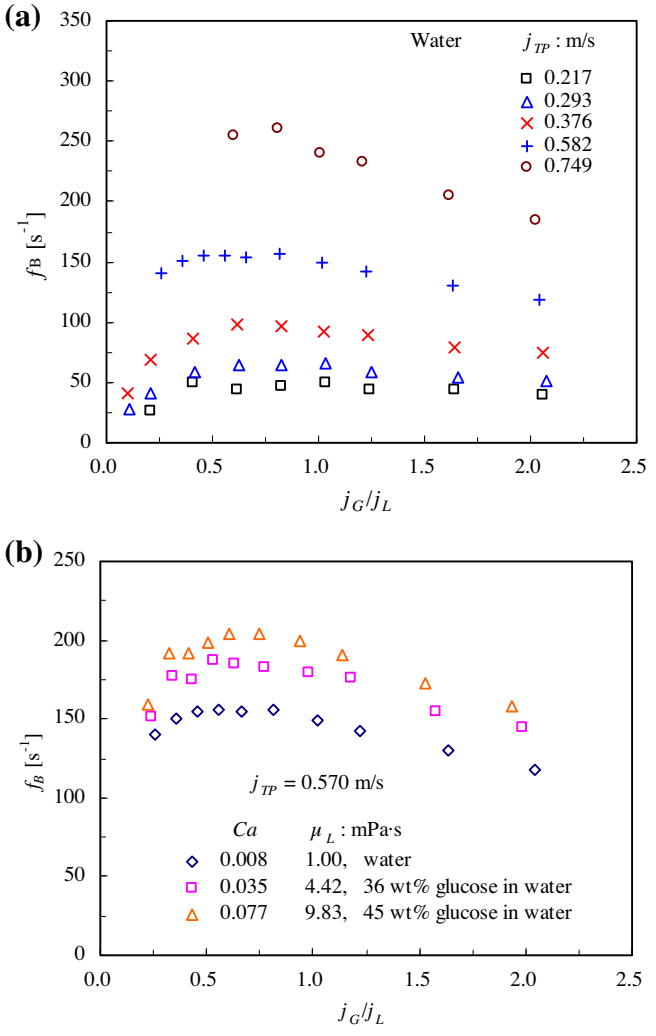

Fig. 11. Effect on the bubble frequency: (a) gas–liquid flow ratio and two-phase mixture velocity; and (b) liquid viscosity.

than about 0.5 and then starts to decrease with the increase of j_G/j_L. This is because that, for a given j_{TP}, an opposite trend is found in t_e and t_r with the increase of j_G/j_L (cf. Fig. 5). This leads to a minimum in the sum of t_e and t_r. It is known that $f_B = 1/(t_e + t_r)$, so the bubble frequency reaches a maximum when the gas–liquid flow ratio is increased above a certain value. For the same j_G/j_L, an increase of j_{TP} leads to an increase in f_B. This is caused by the fact that both t_e and t_r decrease with the increase of j_{TP} (see Fig. 5). From Fig. 11b, f_B is seen to increase with the increase of liquid viscosity for given j_G/j_L and j_{TP}. This could be understood since an increase in viscosity makes the rupture time decrease significantly while it has less pronounced effect on the expansion time (see Fig. 3). Therefore, the total formation time of Taylor bubble decreases with increasing liquid viscosity, which translates into a larger bubble frequency at higher viscosity.

3.4. Shape of Taylor bubble

The Taylor bubble shape in square channels has been extensively studied by many researchers. Kolb and Cerro [41] proposed two bubble shapes as shown in Fig. 12. At $Ca < 0.1$, the bubble is not axisymmetric and flattens out against the tube walls leaving liquid regions in the corners separated by thin flat films at the channel sides. A transition in bubble symmetry occurred at higher Ca, where the whole bubble body becomes cylindrical. They experimentally observed the transitional Ca to be about 0.1 for upward air–silicone oil flow in a square capillary with $d_h = 2$ mm. Thulasidas et al. [42] found out the transitional point at $Ca \approx 0.04$. However, it is difficult to judge the cross-sectional shape of Taylor bubbles in the current microchannel simply on the basis of 2D photos imaged by the high-speed camera. Therefore, the two ideal models (model-1 and model-2) as depicted in Fig. 12 are considered here for a comparison with the current experiments in order to infer the cross-sectional shape of Taylor bubbles produced in our experimental conditions.

Fig. 13 shows 2D shape of Taylor bubbles formed at different Ca. At low Ca, the end of bubble is spherical. With increasing Ca, the front of the bubble becomes sharper and the rear of the bubble tends to be flatter. In our experiments, Ca ranges from 0.003 to 0.030, so the shapes of the front cap and the rear cap do not change very significantly. And we can roughly assume that the bubble has two hemispherical caps. In our experiments, the liquid film thickness (δ) was estimated to be 7.2–29.4 μm which is 1.2–4.9% of the microchannel hydraulic diameter according to Taylor's law [43]:

$$\frac{\delta}{d_h} = \frac{0.67Ca^{2/3}}{1 + 3.35Ca^{2/3}} \tag{16}$$

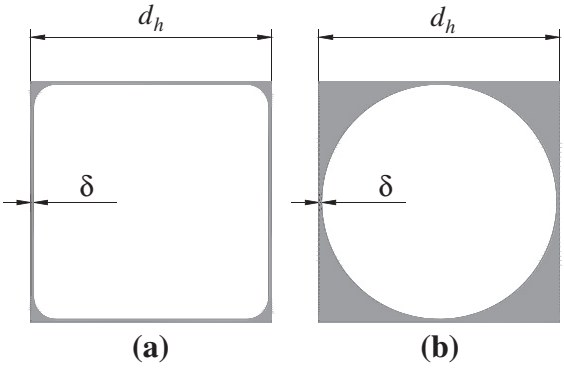

Fig. 12. Cross-sectional shape of Taylor bubble in a square microchannel. (a) model-1: square; and (b) model-2: circular.

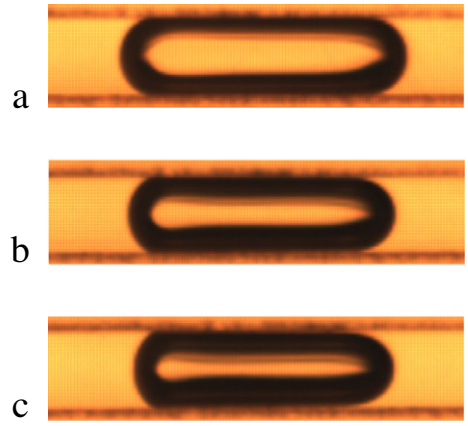

Fig. 13. 2D shapes of Taylor bubble at different Ca. (a) liquid phase: water, $Ca = 0.003$, $j_G = 0.10$ m/s, $j_L = 0.12$ m/s; and (b) liquid phase: 36 wt.% glucose solution in water, $Ca = 0.013$, $j_G = 0.10$ m/s, $j_L = 0.12$ m/s; (c) liquid phase: 45 wt.% glucose solution in water, $Ca = 0.029$, $j_G = 0.10$ m/s, and $j_L = 0.12$ m/s.

Therefore, the liquid film thickness can be neglected during the estimation of the bubble volume (V_B). Two ideal models of the bubble shape are then resorted to as follows:

Model-1: the cross-sectional shape of Taylor bubble body is square as shown in Fig. 12a. By neglecting the liquid film thickness, and assuming that the bubble has two hemispherical caps (with diameters of d_h) and a cuboid body (with a square end, side length of d_h and a height of $(L_B - d_h)$), we can estimate the bubble volume from Eq. (17):

$$V_B = \frac{4}{3}\pi\left(\frac{d_h}{2}\right)^3 + d_h^2(L_B - d_h) = d_h^3\left(\frac{L_B}{d_h} + \frac{\pi}{6} - 1\right) \tag{17}$$

Model-2: the cross-sectional shape of Taylor bubble body is circular as shown in Fig. 12b. By neglecting the liquid film thickness, and assuming that the bubble has two hemispherical caps (with diameters of d_h) and a cylinder body (with a circular end, a diameter of d_h and a height of $(L_B - d_h)$). The bubble volume according to model-2 can be calculated as

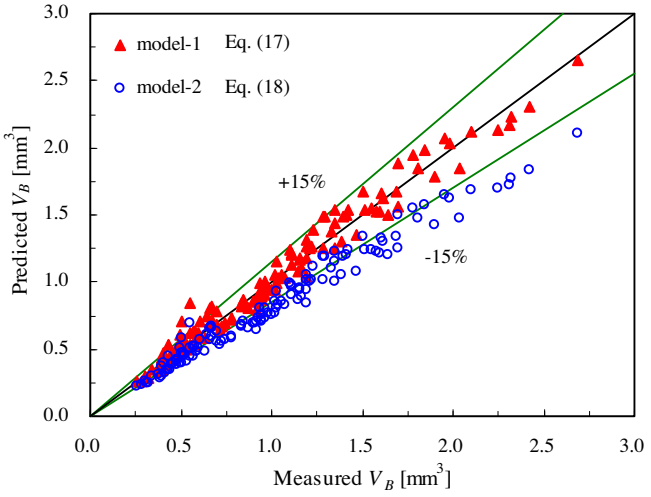

Fig. 14. Comparison between the measured Taylor bubble volume values and the predictions of two models. Liquid phase: water, glucose solution in water (36 wt.% and 45 wt.%). $j_G = 0.106$–0.852 m/s, $j_L = 0.083$–0.415 m/s. In either model, bubble volumes for each gas–liquid system under investigation are shown as one symbol for brevity.

$$V_B = \frac{4}{3}\pi\left(\frac{d_h}{2}\right)^3 + \pi\left(\frac{d_h}{2}\right)^2 (L_B - d_h) = d_h^3\left(\frac{\pi}{4}\frac{L_B}{d_h} - \frac{\pi}{12}\right) \quad (18)$$

In our experiments, V_B can be also measured from

$$V_B = \frac{Q_G}{f_B} \quad (19)$$

where Q_G is the gas volumetric flow rate.

Fig. 14 shows the comparison between the measured values of V_B (calculated by Eq. (19)) and those predicted according to the two models (calculated by Eqs. (17) and (18)). We can see that the predictions according to model-1 agree better with the measured values. The mean relative errors between the measurements and the predictions are 7.5% and 17.4% for model-1 and model-2, respectively. As *Ca* ranges from 0.0026 to 0.030 in our experiments and is below the transition point at which the shape of the bubble body changes from non-axisymmetric to cylindrical [42], the bubble shape should be more reasonably represented by model-1. That is, the bubble body is close to be a cuboid in current operating conditions, which is in accordance with the literature results [42,44].

4. Conclusions

Taylor bubble formation process in a microchannel with a converging shape mixing junction has been experimentally investigated. The effect of liquid viscosity, gas–liquid flow ratio and two-phase mixture velocity on the bubble formation process, bubble length and bubble frequency were studied. The bubble shape was also discussed. Based on the results of this study, the following conclusions can be drawn:

(1) A perfectly periodic Taylor bubble formation process was observed to consist of two steps including the expansion step and the rupture step. The expansion time decreases with an increase in the liquid viscosity, gas–liquid flow ratio and two-phase mixture velocity. The rupture time decreases with an increase in the liquid viscosity, and two-phase mixture velocity under our experimental conditions, while it increases linearly with gas–liquid flow ratio.
(2) The bubble length could be approximated by the product of the rupture time and the two-phase mixture velocity. An empirical correlation was further developed to address the influence of parameters such as liquid viscosity, gas–liquid flow ratio and two-phase mixture velocity on the bubble length produced in the current microfluidic geometry, which can explain the experimental measurements fairly well.
(3) The bubble frequency reaches a maximum when the gas–liquid flow ratio is increased from about 0.5–1 at a given two-phase mixture velocity. The increase of liquid viscosity leads to an increase in the bubble frequency.
(4) The cross-sectional shape of Taylor bubble body is close to square at low *Ca*.

Acknowledgments

The work was financially supported by research grants from the National Natural Science Foundation of China (NSFC) (Nos. 21225627 and 21106141) and the framework of the Sino-French project MIGALI via the NSFC (No. 20911130358).

References

[1] M.N. Kashid, L. Kiwi-Minsker, Microstructured reactors for multiphase reactions: state of the art, Ind. Eng. Chem. Res. 48 (2009) 6465–6485.
[2] J. Hou, G. Qian, X. Zhou, Gas–liquid mixing in a multi-scale micromixer with arborescence structure, Chem. Eng. J. 167 (2011) 475–482.
[3] Y. Zhang, Y. Hu, H. Wu, Design and simulation of passive micromixers based on capillary, Microfluid. Nanofluid. (2012) 1–10.
[4] J.L.H. Chau, A.Y.L. Leung, K.L. Yeung, Zeolite micromembranes, Lab Chip 3 (2003) 53–55.
[5] N. Oozeki, S. Ookawara, K. Ogawa, P. Löb, V. Hessel, Characterization of microseparator/classifier with a simple arc microchannel, AlChE J. 55 (2009) 24–34.
[6] S.M. Lai, R. Martin-Aranda, K.L. Yeung, Knoevenagel condensation reaction in a membrane microreactor, Chem. Commun. (2003) 218–219.
[7] K.L. Yeung, X.F. Zhang, W.N. Lau, R. Martin-Aranda, Experiments and modeling of membrane microreactors, Catal. Today 110 (2005) 26–37.
[8] P. Lang, M. Hill, I. Krossing, P. Woias, Multiphase minireactor system for direct fluorination of ethylene carbonate, Chem. Eng. J. 179 (2012) 330–337.
[9] E. Livak-Dahl, I. Sinn, M. Burns, Microfluidic chemical analysis systems, in: J.M. Prausnitz (Ed.), Annual Review of Chemical and Biomolecular Engineering, vol. 2, Annual Reviews, Palo Alto, 2011, pp. 325–353.
[10] J. Yue, L. Luo, Y. Gonthier, G. Chen, Q. Yuan, An experimental investigation of gas–liquid two-phase flow in single microchannel contactors, Chem. Eng. Sci. 63 (2008) 4189–4202.
[11] T.C. Thulasidas, M.A. Abraham, R.L. Cerro, Dispersion during bubble-train flow in capillaries, Chem. Eng. Sci. 54 (1999) 61–76.
[12] G. Berčič, A. Pintar, The role of gas bubbles and liquid slug lengths on mass transport in the Taylor flow through capillaries, Chem. Eng. Sci. 52 (1997) 3709–3719.
[13] J.M. van Baten, R. Krishna, CFD simulations of wall mass transfer for Taylor flow in circular capillaries, Chem. Eng. Sci. 60 (2005) 1117–1126.
[14] A. Gunther, S.A. Khan, M. Thalmann, F. Trachsel, K.F. Jensen, Transport and reaction in microscale segmented gas–liquid flow, Lab Chip 4 (2004) 278–286.
[15] B.K.H. Yen, A. Günther, M.A. Schmidt, K.F. Jensen, M.G. Bawendi, A microfabricated Gas–liquid segmented flow reactor for high-temperature synthesis: the case of CdSe quantum dots, Angew Chem. Int. Ed. 44 (2005) 5447–5451.
[16] S.A. Khan, A. Günther, M.A. Schmidt, K.F. Jensen, Microfluidic synthesis of colloidal silica, Langmuir 20 (2004) 8604–8611.
[17] V.S. Cabeza, S. Kuhn, A.A. Kulkarni, K.F. Jensen, Size-controlled flow synthesis of gold nanoparticles using a segmented flow microfluidic platform, Langmuir 28 (2012) 7007–7013.
[18] T. Yasukawa, W. Ninomiya, K. Ooyachi, N. Aoki, K. Mae, Enhanced production of ethyl pyruvate using gas–liquid slug flow in microchannel, Chem. Eng. J. 167 (2011) 527–530.
[19] J.J.W. Bakker, M.M.P. Zieverink, R. Reintjens, F. Kapteijn, J.A. Moulijn, M.T. Kreutzer, Heterogeneously catalyzed continuous-flow hydrogenation using segmented flow in capillary columns, Chem. Cat. Chem. 3 (2011) 1155–1157.
[20] S.R.A. de Loos, J. van der Schaaf, M. de Croon, T.A. Nijhuis, J.C. Schouten, Heterogeneous catalysis in a microchannel using a layer of carbon nanofibers on the channel wall, Chem. Eng. J. 179 (2012) 242–252.
[21] S. Haase, T. Bauer, New method for simultaneous measurement of hydrodynamics and reaction rates in a mini-channel with Taylor flow, Chem. Eng. J. 176–177 (2011) 65–74.
[22] P. Garstecki, M.J. Fuerstman, H.A. Stone, G.M. Whitesides, Formation of droplets and bubbles in a microfluidic T-junction – scaling and mechanism of break-up, Lab Chip 6 (2006) 437–446.
[23] M. De Menech, P. Garstecki, F. Jousse, H.A. Stone, Transition from squeezing to dripping in a microfluidic T-shaped junction, J. Fluid Mech. 595 (2008) 141–161.
[24] A.R. Abate, P. Mary, V. van Steijn, D.A. Weitz, Experimental validation of plugging during drop formation in a T-junction, Lab Chip 12 (2012) 1516–1521.
[25] M.T. Kreutzer, F. Kapteijn, J.A. Moulijn, J.J. Heiszwolf, Multiphase monolith reactors: chemical reaction engineering of segmented flow in microchannels, Chem. Eng. Sci. 60 (2005) 5895–5916.
[26] J.M. van Baten, R. Krishna, CFD simulations of mass transfer from Taylor bubbles rising in circular capillaries, Chem. Eng. Sci. 59 (2004) 2535–2545.
[27] J. Yue, L. Luo, Y. Gonthier, G. Chen, Q. Yuan, An experimental study of air–water Taylor flow and mass transfer inside square microchannels, Chem. Eng. Sci. 64 (2009) 3697–3708.
[28] D. Qian, A. Lawal, Numerical study on gas and liquid slugs for Taylor flow in a T-junction microchannel, Chem. Eng. Sci. 61 (2006) 7609–7625.
[29] V. van Steijn, M.T. Kreutzer, C.R. Kleijn, Mu-PIV study of the formation of segmented flow in microfluidic T-junctions, Chem. Eng. Sci. 62 (2007) 7505–7514.
[30] J. Tan, S.W. Li, K. Wang, G.S. Luo, Gas–liquid flow in T-junction microfluidic devices with a new perpendicular rupturing flow route, Chem. Eng. J. 146 (2009) 428–433.
[31] R. Xiong, J.N. Chung, Bubble generation and transport in a microfluidic device with high aspect ratio, Exp. Therm. Fluid Sci. 33 (2009) 1156–1162.
[32] T. Fu, Y. Ma, D. Funfschilling, C. Zhu, H.Z. Li, Squeezing-to-dripping transition for bubble formation in a microfluidic T-junction, Chem. Eng. Sci. 65 (2010) 3739–3748.
[33] T. Cubaud, M. Tatineni, X. Zhong, C.-M. Ho, Bubble dispenser in microfluidic devices, Phys. Rev. E 72 (2005) 037302.
[34] N. Dietrich, S. Poncin, N. Midoux, H.Z. Li, Bubble formation dynamics in various flow-focusing microdevices, Langmuir 24 (2008) 13904–13911.

[35] T. Fu, D. Funfschilling, Y. Ma, H. Li, Scaling the formation of slug bubbles in microfluidic flow-focusing devices, Microfluid. Nanofluid. 8 (2010) 467–475.
[36] R. Xiong, B. Mo, N.C. Jacob, et al., Formation of bubbles in a simple co-flowing micro-channel, J. Micromech. Microeng. 17 (2007) 1002.
[37] T. Fu, Y. Ma, D. Funfschilling, H.Z. Li, Bubble formation and breakup mechanism in a microfluidic flow-focusing device, Chem. Eng. Sci. 64 (2009) 2392–2400.
[38] H. Tsuge, Y. Nakajima, K. Terasaka, Behavior of bubbles formed from a submerged orifice under high system pressure, Chem. Eng. Sci. 47 (1992) 3273–3280.
[39] D.H. Yoo, H. Tsuge, K. Terasaka, K. Mizutani, Behavior of bubble formation in suspended solution for an elevated pressure system, Chem. Eng. Sci. 52 (1997) 3701–3707.
[40] S. Laborie, C. Cabassud, L. Durand-Bourlier, J.M. Lainé, Characterisation of gas–liquid two-phase flow inside capillaries, Chem. Eng. Sci. 54 (1999) 5723–5735.
[41] W.B. Kolb, R.L. Cerro, Coating the inside of a capillary of square cross section, Chem. Eng. Sci. 46 (1991) 2181–2195.
[42] T.C. Thulasidas, M.A. Abraham, R.L. Cerro, Bubble-train flow in capillaries of circular and square cross section, Chem. Eng. Sci. 50 (1995) 183–199.
[43] P. Aussillous, D. Quere, Quick deposition of a fluid on the wall of a tube, Phys. Fluids 12 (2000) 2367–2371.
[44] T. Taha, Z.F. Cui, CFD modelling of slug flow inside square capillaries, Chem. Eng. Sci. 61 (2006) 665–675.